Article

Feasibility Simulation of 3D Benchtop Multi-Pinhole X-ray Fluorescence Computed Tomography with Two Novel Geometries

Binqiang Ye [1,†], Luzhen Deng [1,*,†], Shanghai Jiang [2], Sijun Cao [3], Ruge Zhao [3] and Peng Feng [3,*]

[1] College of Artificial Intelligence, Chongqing University of Technology, Chongqing 401135, China; ybq@cqut.edu.cn

[2] Chongqing Key Laboratory of Optical Fiber Sensor and Photoelectric Detection, Chongqing University of Technology, Chongqing 400054, China

[3] Key Laboratory of Optoelectronic Technology & Systems (Ministry of Education), Chongqing University, Chongqing 400044, China

* Correspondence: dlz@cqu.edu.cn (L.D.); coe-fp@cqu.edu.cn (P.F.)

† These authors contributed equally to this work.

Abstract: In this work, we developed and validated two novel imaging geometries of benchtop multi-pinhole X-ray fluorescence computed tomography (XFCT) systems with Geant4 Toolkit. One of the Monte Carlo (MC) models utilized a fan beam source to illuminate a single slice of the object, a detector and a multi-pinhole collimator to image each slice's X-ray fluorescence (XRF). The other model consisted of a cone-beam X-ray source (designed as a 5 mm wide fan beam to reduce simulation time) to scan the whole object, two detectors and two multi-pinhole collimators to image the emissions. The phantom used in the simulations included four sections, each with three cone-shaped gold nanoparticle (GNP) inserts (5 mm in height, 3 mm in diameter across the top) with center-to-center distances of 4 mm, 4.5 mm and 4.86 mm. The GNPs concentration was 0.1 wt. %, 0.3 wt. %, 0.5 wt. % and 0.7 wt. %, respectively. The diameter of the multi-pinhole collimator was 1 mm. Performance was evaluated for pinhole-detector-distance (PDD) of 5 cm, 3.5 cm and 2.5 cm, and the results for different object layers and for single pinhole and multi-pinhole (9 pinholes) imaging were compared. The data showed that results worsened with decreasing GNPs insert diameters and with decreasing PDD (object-pinhole-distance was fixed). The multi-pinhole configurations performed better than a single pinhole. The detection limit for the first multi-pinhole operation was 0.21 wt. %; the second was 0.24 wt. %. Detection limits for the single pinhole were 0.32 wt. % and 0.35 wt. %, respectively. The first MC model could acquire 2D slice images of the object without rotation and the second MC model could image the 3D object efficiently. These two novel multi-pinhole systems could potentially provide a bioimaging modality for nanomedical applications.

Keywords: Geant4; Monte Carlo simulation; multi-pinhole; X-ray fluorescence computed tomography

1. Introduction

X-ray fluorescence computed tomography (XFCT) is a well-known technique for providing quantitative identification and spatial distributions of trace elements, generally metals such as Au, by collecting X-ray fluorescence (XRF) [1,2] emitted from the sample and mapping such elements simultaneously. XFCT was first proposed by Boisseau in 1986 using synchrotron sources [3]. Synchrotron-based XFCT [4–6] is most commonly used in traditional tomographic geometry due to the high brilliance and collimation of synchrotron X-rays. In recent years, the benchtop XFCT imaging system has shown that it could be a promising imaging modality due to the laboratory availability of polychromatic X-ray sources [7–10]. The group of Cho was the first to use a polychromatic pencil X-ray beam to excite the XRF signal in a Monte Carlo (MC) study [7]. Later on, they demonstrated the

feasibility of the benchtop XFCT using a polychromatic cone-beam experimentally [9]. Since then, numerous studies have been performed to improve the performance of benchtop XFCT: the first demonstration of multiplexed XFCT imaging by the group of Xing [11], postmortem imaging of a tumor-bearing mouse by the group of Cho et al. [10] They translated the parallel collimated detector to acquire each projection, and noted that a 1D array of parallel collimated detectors could be used to reduce the scanning time and a 2D collimated array would allow for simultaneous multi-slice acquisition. However, the design of the long parallel collimators, which are difficult to miniaturize, limited the improvement of the spatial resolution. Considerable improvement in 3D imaging is still required to accomplish while meeting realistic constraints for scan time, spatial resolution, and detection limit. New XFCT imaging systems [12–19] were proposed to improve image quality: pinhole collimated and slit collimated systems were proposed by the group of Fu [18], multi-pinhole collimated and multi-slit collimated systems were simulated by the group of Meng [19], and a pinhole collimated system and a multi-pinhole collimated system were demonstrated experimentally by the group of Sasaya [15,16]. Their studies used monochromatic X-ray sources. Jung's group conducted an MC study on pinhole imaging without rotation and reconstruction, utilizing polychromatic X-rays as the excitation source [14].

However, the performance of pinhole collimated XFCT systems with polychromatic X-ray beams still needs to be improved. We recently proposed a Geant4-based multi-pinhole benchtop XFCT imaging system that enabled faster data acquisition by obtaining nine projections simultaneously through nine pinholes and obtained a 2D XFCT image of a PMMA phantom without rotation [12]. However, in that MC mode, the width of the fan beam and the detector material was not considered, and layers had to be scanned sequentially to obtain 3D distributions of the phantom. However, the effects that pinhole diameter had on the reconstruction quality can still provide a reference for future multi-pinhole designs.

In this study, we focused on developing different MC models to provide 3D distributions of the phantom and provide a referee for future multi-pinhole set-up design. A polychromatic X-ray source and the width of the fan beam and the detector material were included in the simulations to mimic the experiments. The pinhole diameter used in all the simulations in this study was 1 mm, which our previous study demonstrated to be ideal for resolution and signal-to–noise ratio(SNR) [12]. We assessed the performance of two MC models by comparing the full-width-at-half-maximum (FWHM) [20] and the contrast-to-noise ratio (CNR) values for both single-pinhole and multi-pinhole configurations (with nine pinholes) [21,22].

2. Material and Methods

2.1. MC Model

The MC models were developed using the Geant4 toolkit (Release 10.04). Two novel geometries were considered in this study, illustrated schematically in Figure 1. In the first, shown on the left (Figure 1a), a 0.45 mm wide fan beam of X-rays illuminated a single slice through the object, inducing the emission of characteristic X-rays from that slice. A detector composed of 235×235 CdTe (47% Cd and 53% Te, available in the Geant4 material database) crystals was placed parallel to that object slice. We positioned a multi-pinhole collimator (depicted in Figure 2a–c) between the detector and the phantom. The vertical center-to-center distance (VCCD)and horizontal center-to-center distance (HCCD) of the holes were both 1.65 cm. In the second geometry, shown on the right (Figure 1b), a cone beam (designed as a 5 mm wide fan beam to reduce simulating time) of X-rays illuminated the whole object, inducing the emission of characteristic X-rays from the entire object. These emissions were detected by two detectors, each containing 105×235 CdTe crystals. The detectors were placed perpendicular to the surface of the object. Two multi-pinhole collimators (Figure 2a–c) were situated between the detector and the phantom. The VCCD of the holes was 0.865 cm and the HCCD of the holes was 1.65 cm.
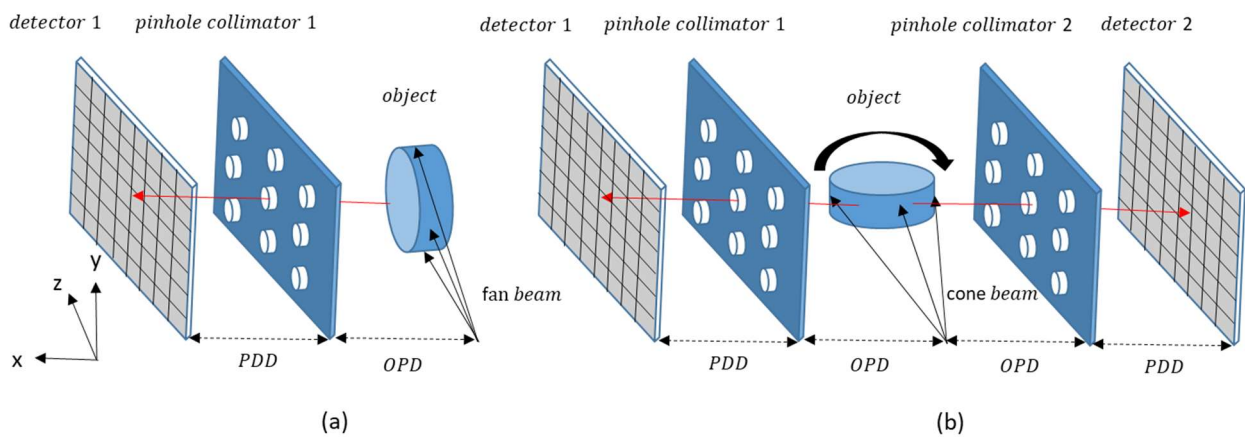
Figure 1. Schematic for the current MC models with the system components. (**a**) PMP and (**b**) MP geometries. The red arrows signify the emission of XRF photons from the phantom that strike the detectors.
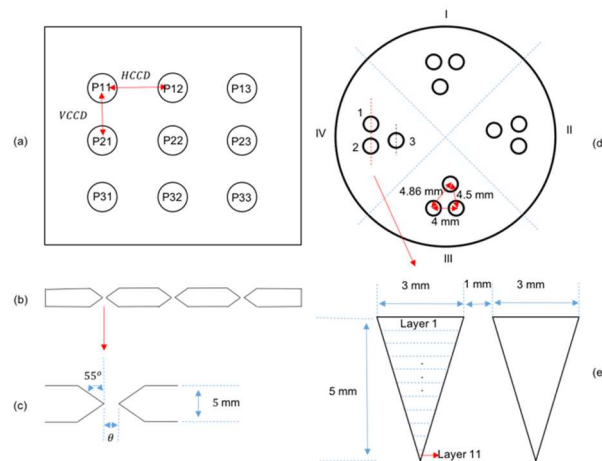
Figure 2. Layout of multi-pinhole collimator and PMMA phantom. (**a**) Perpendicular view of the lead plate containing nine pinholes; (**b**) cross-section of the lead plate containing the centers of the pinholes; (**c**) cross-section of a pinhole; (**d**) phantom and (**e**) vertical section of the phantom along the red dashed line.

For both geometries, the source spectra used in the simulations were generated beforehand by directing 125 kVp electrons at a tungsten target. The source was then filtered through a 0.8 mm thick beryllium window and a 1.8 mm thick tin. The object scanned was a Polymethyl Methacrylate (PMMA) phantom (Figure 2d,e) located 15 cm away from the source. The object-pinhole-distance (OPD) and the original pinhole-detector-distance (PDD) were 5 cm. The crystal size was 0.25 mm × 0.25 mm, with a center-to-center distance of 0.45 mm (the gap between the crystals was filled with air). The detector thickness was 1 mm.

The multi-pinhole collimators were made up of a 5 mm thick lead plate and nine pinholes arranged in 3 rows with 3 pinholes in each row. The pinholes had a cone-shaped profile with an acceptance angle of 110°, which was chosen to cover the object. The VCCD and HCCD of the holes were chosen to avoid projection overlaps. For ease of comparison, PMP and MP are used to stand for the first and second geometries individually.

2.2. Phantom

A single PMMA phantom measuring 3 cm in diameter and 0.5 cm in height was used in the simulations. It contained 4 sections, and each section had 3 cone shape GNPs inserts (Figure 2d). The GNPs insert bottom to top diameters changed from 0 to 3 mm (Figure 2e).

The GNPs inserts center-to-center distances in a section were 4 mm, 4.5 mm and 4.86 mm. The GNPs concentration was 0.1 wt. % in Section 1, 0.3 wt. % in Section 2, 0.5 wt. % in Section 3 and 0.7 wt. % in Section 4.

2.3. Data Acquisition and Processing

The MC simulation, which takes 200 min (10 computers with Inter i7-107000K CPU@3.80GHx16 were run simultaneously), utilized 100 billion photons, with particle interactions and transportation modeled through the Penelope low energy electromagnetic physics list. This list encompasses photon transport, as well as the Compton, photoelectric and Rayleigh scattering effects.

For the PMP geometry, the object was moved along the line between the object and detector in steps of 0.45 mm (the same as the beam width). There were 11 steps to almost cover the object. For the MP geometry, the object was rotated 15 (12° increment each) times to acquire 15 projections. For both geometries, the detectors were moved toward the object and the PDD was changed from 5 cm to 3.5 cm and 2.5 cm.

The energy deposited in the CdTe crystals was scored, and spectrums were generated with perfect charge collection. The detector material CdTe would cause escape events (if the incident photon energy is greater than Cd k-shell absorption energy, i.e., 23.2 and 26.1 keV, and Te absorption energy, i.e., 27.5 and 31 keV, XRF emissions and the detected spectrum were distorted) during simulations. The stripping algorithm [23,24] was applied to correct the X-ray spectra detected by the CdTe detector.

To estimate the Compton background, a third-order polynomial ($p(x) = p_1 x^3 + p_2 e^2 + p_3 x + p_4$. For the MP geometry, the whole projection was acquired from 15 rotations, and it also can be divided into 9 sub-projections through 9 pinholes. Reconstruction of the image could be performed either from the entire projection or from each individual sub-projection. The object could be divided into 11 layers (shown in Figure 2e) according to 11 steps in the PMP geometry scan.

The reconstructions for all simulations were performed using the maximum-likelihood expectation maximization (MLEM) method [8,25,26]:

$$f_i^{m+1} = \frac{f_i^m}{\sum_j M_{i,j}} \times \sum_j M_{i,j} \frac{p_j}{\sum_i M_{i,j} f_i^m} \tag{1}$$

In the *mth* iteration, f_i^m represents the *ith* pixel intensity of the reconstructed image f, while p_j refers to the element of projection p that describes the XRF signal detected by the *jth* detector. The system matrix $M_{i,j}$ is an element of M that indicates the probability of creating a fluorescence photon at f_i and detecting it in the projection element p_j. To construct the system matrix, an attenuation correction based on the a priori attenuation coefficient of PMMA [27] was applied at the intensity-weighted mean energy of the excitation beam (85 keV) and at an XRF photon energy (68 keV).

$$M_{i,j} = \frac{\exp(-\int_A^B \mu_{beam(l_1)} dl_1) \exp(-\int_B^C \mu_{gold(l_2)} dl_2)}{|d|^2} \tag{2}$$

The attenuation coefficients of the source photons and gold K_α photons are represented respectively by μ_{beam} and μ_{gold}. The segment from entering object point A to pixel point B is denoted by l_1, while the segment from pixel point B to exiting object point C is represented by l_2. The distance from pixel point B to the detector is indicated by d. To facilitate visual comparison of the reconstructed images, we reduced the pixel size from 0.45 mm × 0.45 mm to 0.225 mm × 0.225 mm using bilinear interpolation, which is a MATLAB built-in function.

2.4. Image Analysis

To compare the spatial resolution, we calculated the FWHM [20,28] along the black dashed line shown in Figure 2d. The FWHM was determined to be 2.355σ, where σ represents the standard deviation of the Gaussian fitting function.

To determine the CNR [21,22], we calculated the ratio between the difference in mean values of each region of interest (ROI) with the background and the standard deviation of the background.

$$CNR = \frac{\overrightarrow{f}_{ROI} - \overrightarrow{f}_{BK}}{\sqrt{\sigma_{BK}^2}} \tag{3}$$

The variables $\overrightarrow{f}_{ROI}$ and $\overrightarrow{f}_{BK}$ represent the mean values of ROI and the background, while σ_{BK}^2 refers to the variance of the background.

In this study, the ROI area is all the GNP areas in each section of the phantom. Following the Rose criterion, a CNR of 5 was chosen to determine the detection limit.

3. Result

3.1. Comparison of Multi-Pinholes in Different Layers

For the 5 cm PDD setting, the CNR was calculated and Figure 3a shows the relationship between GNP concentration and CNR for the third layer of MP geometry. As expected, the relationship is sufficiently linear. The detection limit (CNR = 5) was determined for different layers in two geometries and Figure 3b depicts the changes. For both geometries, the detection limit values were similar and increased with decreasing insert diameters. The detection limit values of PMP geometry were slightly lower than that of MP geometry when the layers were smaller than 6 (insert diameters were bigger than 1.515 mm), while they were higher when the layers were bigger than 6 (insert diameters were smaller than 1.515 mm). Figure 4a,e illustrate the vertical sectional images of nine pinholes of two geometries. Two inserts were separated from the fourth layer (2.055 mm diameter/1.945 mm gap) in Figure 4a, and from the second layer (2.595 mm diameter/1.405 mm gap) in Figure 4e. However, Figure 4e had more artifacts than Figure 4a.
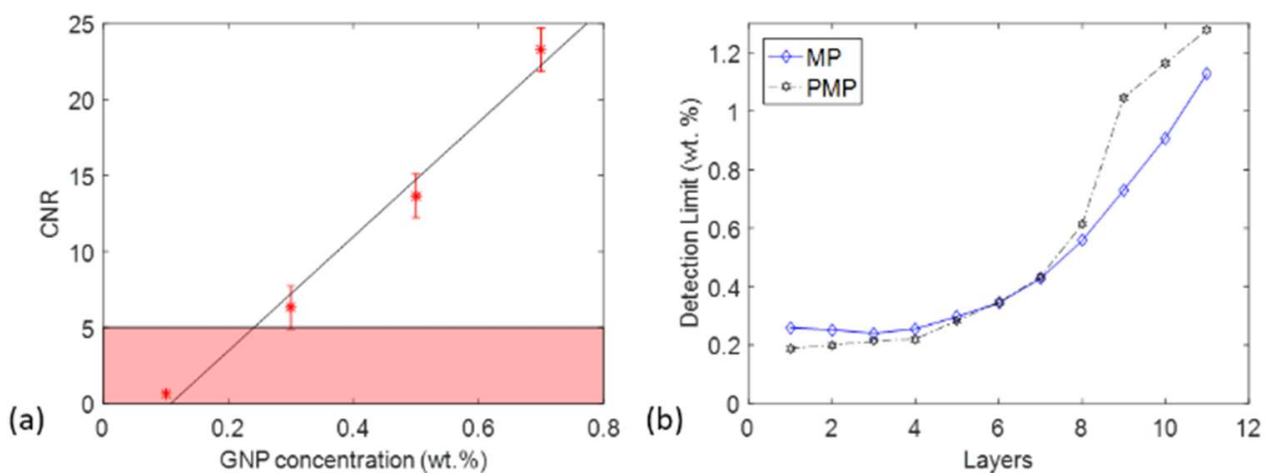
Figure 3. (**a**) CNR as a function of GNP concentration for the third layer of MP geometry; (**b**) detection limit of two geometries in different layers. The shaded area represents CNR < 5, which was considered to be below the detection threshold. The intersection of the linear fit with the shaded region represents the detection limit under that condition.
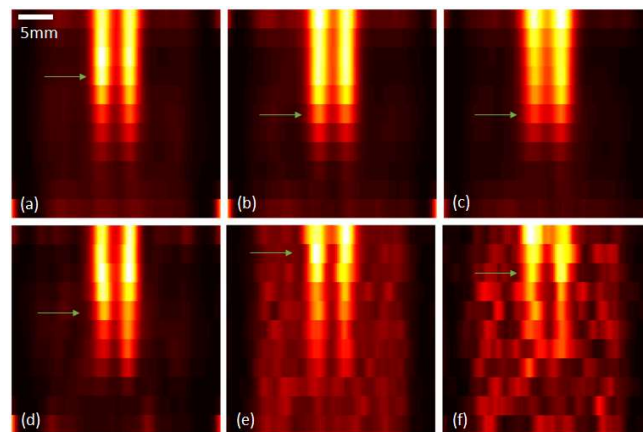
Figure 4. Vertical sectional images of nine pinholes of MP geometry with (**a**) 5 cm OPD and 5 cm PDD, (**b**) 5 cm OPD and 3.5 cm PDD, (**c**) 5 cm OPD and 2.5 cm PDD, (**d**) single pinhole of MP geometry with 5 cm OPD and 5 cm PDD, (**e**) 9 pinholes and (**f**) single pinhole of PMP geometry with 5 cm OPD and 5 cm PDD. Results are shown along the red dashed line in Figure 2d. Single pinhole is P22 in Figure 2a. The green arrows point to the layers the two inserts are separating.

3.2. Comparison of Multi-Pinholes for Different Magnification

Further studies were performed by changing the PDD from 5 cm to 3.5 cm and 2.5 cm. Figure 4a–c show the corresponding vertical sectional images of nine pinholes of MP geometry. Figure 5 represents the reconstructed images of the third layer in both PMP and MP geometries with different PDD. Corresponding FWHM and detection limit were plotted in Figure 6. It was found that the FWHM and detection limit values increased with decreasing PDD (OPD was fixed). PMP geometry had lower FWHM and detection limit values than MP geometry. Two inserts were separated from the fourth layer for 5 cm PDD (Figure 4a); they were clearly separated and almost separated from the fifth layer for 3.5 cm (Figure 4b) and 2.5 cm (Figure 4c) PDD, respectively. For the third layer of nine pinholes in MP geometry (Figure 5b,f,j), the first and second inserts were connected for all PDD settings; the second and the third inserts were separated for 5 cm PDD (Figure 5b), and connected for 3.5 cm (Figure 5f) and 2.5 cm (Figure 5j) PDD; the first and third inserts were almost separated for 3.5 cm PDD (Figure 5f), while were connected with 2.5 cm PDD (Figure 5j). For the third layer of nine pinholes in PMP geometry, all the inserts were separated for 5 cm PDD (Figure 5c); only the first and second inserts were connected for 3.5 cm PDD (Figure 5g); all the inserts were connected with 2.5 cm PDD (Figure 5k).

3.3. Comparison of Single Pinholes and Multi-Pinhole

In PMP geometry, Figure 7a illustrates the projection of the third layer of the PMMA phantom. Figure 8a shows the projection of the PMMA phantom from detector 1 in MP geometry with 0-degree rotation.

The channels for each pinhole (labeled in Figure 2a) are distinctly separated with no overlapping images. Although the PMP geometry projection provides a 2D slice of the structure whose positions are opposite from the object, the image is noisy with poor resolution. Figure 7b shows reconstructed images obtained from the individual sub-projections depicted in Figure 7a. The complete projection of MP geometry was achieved by combining the projections from all 15 rotations, and Figure 8b illustrates the images reconstructed from the sub-projections for each individual pinhole. The position of the pinhole appears to affect the image quality, as illustrated by Figure 9, which displays the corresponding CNR values and confirms the dependence of CNR on the pinhole position. The CNR of PMP geometry is lower than that of MP geometry.
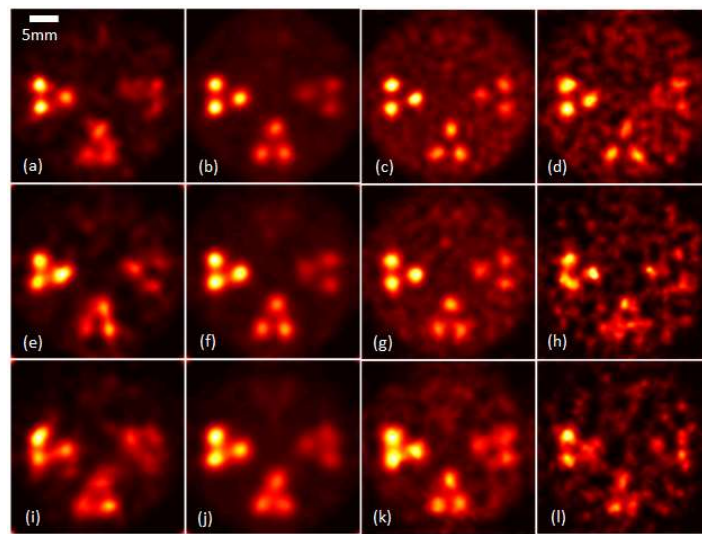
Figure 5. Reconstructed images acquired using (**a**) single pinhole and (**b**) nine pinholes of MP geometry with 5 cm OPD and 5 cm PDD; (**c**) single pinhole and (**d**) nine pinholes of PMP geometry with 5 cm OPD and 5 cm PDD; (**e**) single pinhole and (**f**) nine pinholes of MP geometry with 5 cm OPD and 3.5 cm PDD; (**g**) single pinhole and (**h**) nine pinholes of PMP geometry with 5 cm OPD and 3.5 cm PDD; (**i**) single pinhole and (**j**) nine pinholes of MP geometry with 5 cm OPD and 2.5 cm PDD; (**k**) single pinhole and (**l**) nine pinholes of PMP geometry with 5 cm OPD and 2.5 cm PDD. Results are shown for the third layer of the object. Single pinhole is P22 in Figure 2a.
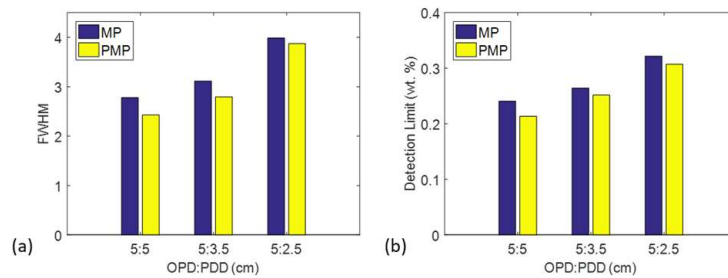
Figure 6. (**a**) FWHM and (**b**) detection limit for PMP and MP geometries for different OPD and PDD values. Results are shown for the nine pinholes.
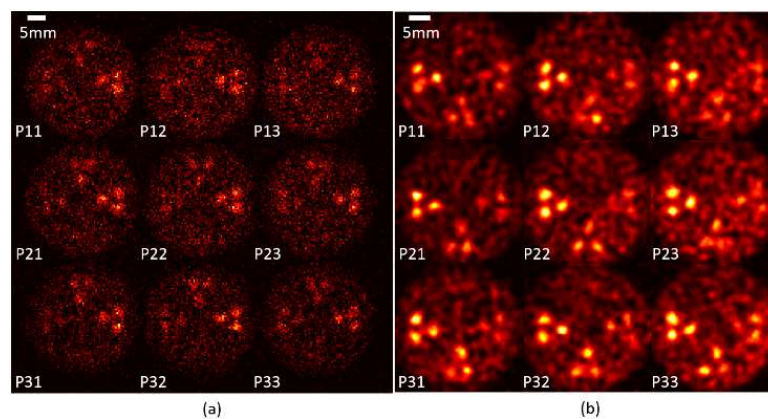
Figure 7. (**a**) Projection and (**b**) reconstructed images for single pinholes of PMP geometry.
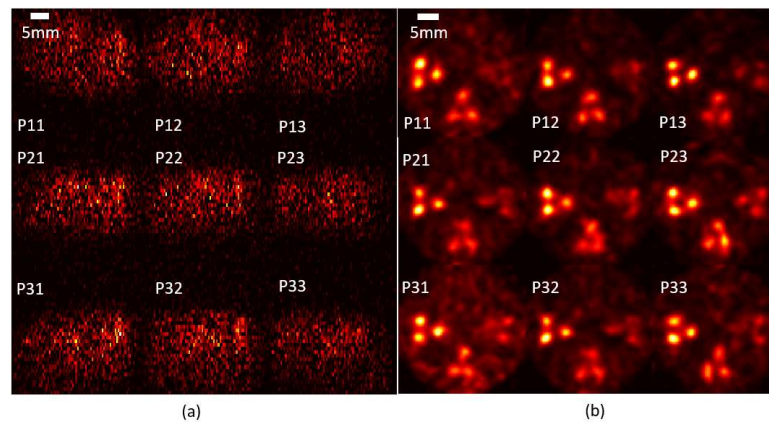
Figure 8. (**a**) Projection and (**b**) reconstructed images for single pinholes of MP geometry.
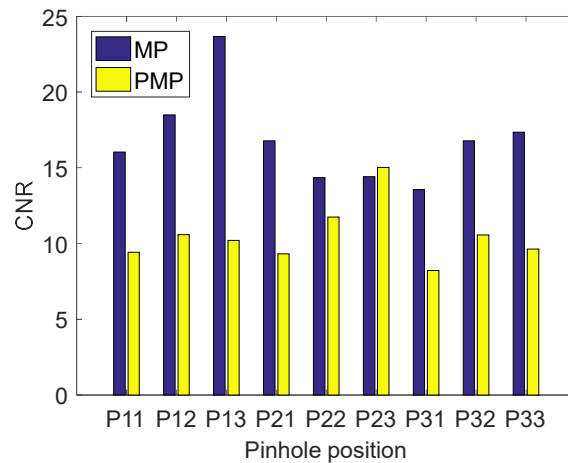

Figure 9. CNR of reconstructed images in PMP and MP geometries.

Figure 5a,d,e,h,i,l depict the images of the third layer from single pinholes (P22) in MP and PMP geometries, respectively. Compared with the images from multi-pinhole (Figure 5b,c,f,g,j,k), the images from single pinholes contain more artifacts and the shape of GNP areas are less clear.

Table 1 presents the detection limit values for single and multi-pinhole configurations in both MP and PMP geometries, corresponding to different OPD and PDD values. As anticipated, the number of pinholes had a discernible impact on the detection limit values. In the case of MP geometry, the multi-pinhole configuration exhibited a lower detection limit of 0.24 wt. %, while the single pinhole configuration had a detection limit of 0.32 wt. %. Similarly, for PMP geometry, the multi-pinhole configuration showed a lower detection limit of 0.21 wt. %, while the single pinhole configuration had a detection limit of 0.35 wt. %. The detection limit values of PMP geometry were slightly lower than those of MP geometry for multi-pinhole configurations, while they were slightly higher for single-pinhole configurations.

Table 1. Detection limit (wt. %) for single pinhole and multi-pinhole configurations with magnifications in both MP and PMP geometries. Results are shown for the third layer in both geometries.

	MP			**PMP**		
OPD:PDD	5:5	5:3.5	5:2.5	5:5	5:3.5	5:2.5
9PH	0.24	0.26	0.32	0.21	0.25	0.31
1PH	0.32	0.32	0.42	0.35	0.47	0.41

4. Discussion

We have demonstrated the implementations of two novel multi-pinhole systems for 3D XFCT imaging. One (PMP geometry) used a fan beam to scan a slice of the object and a pinhole-collimated detector to obtain the projection, which provides a direct 2D slice image. Three-dimensional images were acquired by scanning the object layers sequentially. No rotation is required in this mode. The other (MP geometry) used a cone beam (designed as a 5 mm wide fan beam to reduce simulating time) to scan the whole object, and 15 rotations were used in the simulations. The object was only rotated from 0 to π because two detectors were utilized for the MP geometry (the projections from 0 to π in detector 2 are the same as the projections from π to 2π in detector 1). The resolution of PMP geometry is better than that of MP geometry, while the images contain more artifacts in PMP geometry. PMP geometry can improve its resolution and signal–noise ratio by using a smaller source collimator to obtain a thinner beam, but it would take longer to scan all of the object layers sequentially to obtain 3D images. MP geometry could also improve its image quality by increasing the number of rotations, possibly at the expense of increased scan time. Of these two geometries, PMP geometry would be very well suited to image one or several 2D slices due to its efficiency. However, for imaging a long 3D object (the number of layers is more than the number of rotations), MP geometry could be a better choice.

According to our previous study, 1 mm pinhole size performed better than 3.7 mm, 2 mm, 0.5 mm and 0.25 mm in terms of resolution and signal-to-noise [12] in the PMP model when the detector size was 0.45 mm, so 1 mm was used as the pinhole size for all the simulations in this study. The image resolution can be affected by both pinhole diameter and crystal center-to-center distance. We keep the pinhole size and crystal center-to-center distance constant in order to validate the affection of other configurations, such as detector-pinhole distance, etc. In addition, we also need to realize that the ideal pinhole size can be smaller when the detector size is smaller, which makes this setup possible to be used as a bioimaging modality for nanomedical applications. In the future, the relation between image resolution and crystal center-to-center distance can be studied.

In the simulations, CdTe was used as the detector material, which is a common material for XRF detection. Energy deposited in the CdTe crystals was scored, and spectrums were generated with perfect charge collection. It has already been demonstrated that the experimental data can match the Geant4 simulation data by applying the CdTe response function [29]. Exploring different detector response functions to reconcile experimental and simulated data for non-CdTe crystal materials is beyond the scope of the present study but may be explored in future investigations. Figure 7a depicts the 2D slice structure of the object, but the projection is noisy and contains artifacts due to the detector's inability to capture point-to-point information. Therefore, MLEM is necessary for reconstructing PMP geometry simulations. Figures 7b and 8b show varying background regions and CNR for different pinholes, which can be attributed to X-ray scattering, primarily Compton scattering. Better XRF signal extraction methods might be able to solve this problem and improve the detection limit. PDD of 5 cm, 3.5 cm and 2.5 cm were tested in our study, and we demonstrated that 5 cm performed better than the others. It seems that bigger magnification gives better resolution and detection limits, but we also need to be aware that longer PDD requires a bigger detector to image the same field of view of an object. More simulations can be performed to study the performances of bigger magnifications in the future.

5. Conclusions

In this study, we developed and validated two Geant4-based MC models of benchtop multi-pinhole XFCT systems for quantitative imaging of GNP distributions. The study evaluated the image resolution and detection limit of multi-pinhole systems, investigated the performance of multi-pinhole systems with varying magnification, and compared the outcomes of multi-pinhole and single-pinhole systems. For both geometries, the detection limit values increased with decreasing GNP insert diameters; image resolution and

detection limit ability was reduced with decreasing PDD (OPD was fixed). Multi-pinhole systems performed better than single-pinhole systems in terms of detection limits and GNP insert shapes. The PMP geometry in multi-pinhole systems demonstrated superior performance in detecting the concentration of GNPs in solution, achieving a detection limit of 0.21 wt. %, slightly better than that of the MP geometry (0.24 wt. %). It would be more beneficial to use PMP geometry to image one or several 2D slices of an object, while it would be more efficient to use MP geometry to obtain 3D (object with longer length) imaging.

References

1. Cesareo, R.; Viezzoli, G. Trace element analysis in biological samples by using XRF spectrometry with secondary radiation. *Phys. Med. Biol.* **1983**, *28*, 1209–1218. [CrossRef]
2. Pushie, M.J.; Pickering, I.J.; Korbas, M.; Hackett, M.J.; George, G.N. Elemental and chemically specific X-ray fluorescence imaging of biological systems. *Chem. Rev.* **2014**, *114*, 8499–8541. [CrossRef]
3. Boisseau, P.; Grodzins, L. Fluorescence tomography using synchrotron radiation at the NSLS. *Hyperfine Int.* **1987**, *33*, 283–292. [CrossRef]
4. Rust, G.F.; Weigelt, J. X-ray fluorescent computer tomography with synchrotron radiation. *IEEE Trans. Nucl. Sci.* **1998**, *45*, 75–88. [CrossRef]
5. Feng, P.; Cong, W.; Wei, B.; Wang, G. Analytic comparison between X-ray fluorescence CT and K-Edge CT. *IEEE Trans. Bio-Med. Eng.* **2014**, *61*, 975–985. [CrossRef]
6. Cesareo, R.; Mascarenhas, S. A new tomographic device based on the detection of fluorescent X-rays. *Nucl. Instrum. Methods A* **1989**, *277*, 669–672. [CrossRef]
7. Cheong, S.K.; Jones, B.L.; Siddiqi, A.K.; Liu, F.; Manohar, N.; Cho, S.H. X-ray fluorescence computed tomography (XFCT) imaging of gold nanoparticle-loaded objects using 110 kVp X-rays. *Phys. Med. Biol.* **2010**, *55*, 647–662. [CrossRef]
8. Jones, B.L.; Cho, S.H. The feasibility of polychromatic cone-beam X-ray fluorescence computed tomography (XFCT) imaging of gold nanoparti-cle-loaded objects: A Monte Carlo study. *Phys. Med. Biol.* **2011**, *56*, 3719–3730. [CrossRef]
9. Jone, B.L.; Manohar, N.; Reynoso, F.; Karellas, A.; Cho, S.H. Experimental demonstration of benchtop X-ray fluorescence computed tomography (XFCT) of gold nanoparticle-loaded objects using lead-and tin-filtered polychromatic cone-beams. *Phys. Med. Biol.* **2012**, *57*, N457–N467. [CrossRef]
10. Manohar, N.; Reynoso, F.J.; Diagaradjane, P.; Krishnan, S.; Cho, S.H. Quantitative imaging of gold nanoparticle distribution in a tumor-bearing mouse using benchtop X-ray fluorescence com-puted tomography. *Sci. Rep.* **2016**, *6*, 22079. [CrossRef]
11. Kuang, Y.; Pratx, G.; Bazalova, M.; Meng, B.; Qian, J.; Xing, L. First demonstration of multiplexed X-ray fluorescence computed tomography (XFCT) imaging. *IEEE Trans. Med. Imaging* **2013**, *32*, 262–267. [CrossRef] [PubMed]
12. Deng, L.; Wei, B.; He, P.; Zhang, Y.; Feng, P. A geant4-based Monte carlo study of a benchtop multi-pinhole X-ray fluorescence computed tomography imaging. *Int. J. Nanomed.* **2018**, *13*, 7207–7216. [CrossRef] [PubMed]
13. Luo, Y.; Feng, P.; Zhao, R.; Zhang, Y.; An, K.; He, P.; Yan, S.; Zhao, X. Simulation Research of Potential Contrast Agents for X-ray Fluorescence CT with Photon Counting Detector. *Front. Phys.* **2021**, *9*, 686988.
14. Jung, S.; Sung, W.; Ye, S.J. Pinhole X-ray fluorescence imaging of gadolinium and gold nanoparticles using polychromatic X-rays: A Monte Carlo study. *Int. J. Nanomed.* **2017**, *12*, 5805–8517. [CrossRef]
15. Sasaya, T.; Sunaguchi, N.; Hyodo, K.; Zeniya, T.; Takeda, T.; Yuasa, T. Dual-energy fluorescent X-ray computed tomography system with a pinhole design: Use of K-Edge discontinuity for scatter correction. *Sci. Rep.* **2017**, *7*, 44143. [CrossRef]

16. Sasaya, T.; Sunaguchi, N.; Hyodo, K.; Zeniya, T.; Yuasa, T. Multi-pinhole fluorescent X-ray computed tomography for molecular imaging. *Sci. Rep.* **2017**, *7*, 5742. [CrossRef]
17. Zhang, S.; Li, L.; Li, R.; Chen, Z. Full-field fan-beam X-ray fluorescence computed tomography system design with linear-array detectors and pinhole colli-mation: A rapid Monte Carlo study. *Opt. Eng.* **2017**, *56*, 113107. [CrossRef]
18. Fu, G.; Meng, L.G.; Eng, P.; Newville, M.; Vargas, P.; Riviere, P.L. Experimental demonstration of novel imaging geometries for X-ray fluorescence computed tomography. *Med. Phys.* **2013**, *40*, 061903. [CrossRef]
19. Meng, L.J.; Li, N.; La Riviere, P.J. X-ray fluorescence emission tomography (XFET) with novel imaging geometries—A Monte Carlo study. *IEEE Trans. Nucl. Sci.* **2011**, *58*, 3359–3369. [CrossRef]
20. Schlueter, F.J.; Wang, G.; Hsieh, P.S.; Brink, J.A.; Balfe, D.M.; Vannier, M.W. Longitudinal image deblurring in spiral CT. *Radiology* **1994**, *193*, 413–418. [CrossRef]
21. Rose, A. Vision: Human and electronic. In *Applied Solid State Physics*; Plenum Press: New York, NY, USA, 1970; pp. 79–160.
22. Dickerscheid, D.; Lavalaye, J.; Romijn, L.; Habraken, J. Contrast-noise-ratio (CNR) analysis and optimisation of breast-specific gamma imaging (BSGI) acquisition protocols. *EJNMMI Res.* **2013**, *3*, 21–33.
23. Miceli, A.; Thierry, R.; Bettuzzi, M.; Flisch, A.; Hofmann, J.; Sennhauser, U.; Casali, F. Comparison of simulated and measured spectra of an industrial 450 kV X-ray tube. *Nucl. Instrum. Methods A* **2007**, *580*, 123–126. [CrossRef]
24. Redus, R.H.; Pantazis, J.A.; Pantazis, T.J.; Huber, A.C.; Cross, B.J. Characterization of CdTe detectors for quantitative X-ray spectroscopy. *IEEE Trans. Nucl. Sci.* **2009**, *56*, 2524–2532. [CrossRef]
25. Lange, K.; Carson, R. EM reconstruction algorithms for emission and transmission tomography. *J. Comput. Assist. Tomogr.* **1984**, *8*, 306–316.
26. Shepp, L.A.; Vardi, Y. Maximum likelihood reconstruction for emission tomography. *IEEE Trans. Med. Imaging* **1982**, *1*, 113–122. [CrossRef]
27. Guo, J.; Feng, P.; Deng, L.; Luo, Y.; He, P.; Wei, B. Optimization of Detection Angle for Pinhole X-Ray Fluorescence Computed Tomography. *Acta Opt. Sin.* **2020**, *40*, 0111017.
28. Nowotny, R. *XMuDat: Photon Attenuation Data on PC*; IAEANDS-195; Nuclear Data Services: Vienna, Austria, 1998. Available online: http://www-nds.iaea.org/publications/iaea-nds/iaea-nds-0195.htm (accessed on 1 August 1998).
29. Ahmed, M.F.; Yasar, S.; Cho, S. A Monte Carlo Model of a Benchtop X-ray Fluorescence Computed Tomography System and Its Application to Validate a Deconvolution-Based X-ray Fluorescence Signal Extraction Method. *IEEE Trans. Med. Imaging* **2018**, *37*, 2483–2492. [CrossRef]